H1-06/98-544
DESY PRC - 98/05

Proposal for an Upgrade of the H1 Luminosity System and its Associated Electronics for HERA 2000

18 June 1998

Authors

V. Andreev[2], B. Andrieu[4], P. Baranov[2], E. Barrelet[5], A. Belousov[2], V. Boudry[4], A. Busata[4], A. Fomenko[2], N. Gogitidze[2], L. Gorbov[2], A. Lebedev[2], H. Lebbolo[5], S. Levonian[1], E. Malinovski[2], F. Moreau[4], G. Morinaud[4], C. Pascaud[3], J.-P. Pharabod[4], Ch. Renard[4], S. Rusakov[2], I. Sheviakov[2], Y. Soloviev[2], L.N. Shtarkov[2], P. Smirnov[2], A. Specka[4], Ch. de la Taille[3], A. Usik[2] and Y. Vazdik[2]

[1] DESY, Hamburg, Germany
[2] Lebedev Physical Institute, Moscow, Russia
[3] LAL, Université de Paris-Sud, IN2P3-CNRS, Orsay, France
[4] LPNHE, Ecole Polytechnique, IN2P3-CNRS, Palaiseau, France
[5] LPNHE, Universités Paris VI and VII, IN2P3-CNRS, Paris, France

Abstract

HERA will undergo a major upgrade in the year 2000, aiming for a fivefold increase of the instantaneous luminosity. This program has serious implications for the H1 luminosity system, in terms of rates, radiation environment and luminosity measurements. This note describes the proposed changes, which make possible measurement of luminosity in the new conditions at HERA 2000.

1 Introduction

A fast and precise method to measure luminosity at HERA [1, 2, 3] is based on the small angle bremsstrahlung events from the Bethe-Heitler (BH) process:

$$\mathrm{ep} \to \mathrm{ep}\gamma. \tag{1}$$

The measurement of the photons produced in reaction (1) at zero angle by a Photon Detector (PD) is exploited to determine the luminosity value. The detection of the scattered electron at small angles in a set of Electron Taggers (ET) is used for the purpose of cross-checks and calibration. This set of detectors constitutes the so-called luminosity system (or luminometer).

The present H1 luminosity system [1] in the current running conditions at HERA is used to determine integrated ep luminosity off-line with an accuracy of $\sim 1.3\,\%$. It also ensures:

- an online luminosity measurement independent of the operational status of H1,
  - with a precision of a few % once per second for the purpose of the machine monitoring and tuning,
  - with a statistical accuracy of 1 % every 10 seconds for H1 ep physics,
- permanent monitoring of the beam conditions at the interaction point (tilt and position), making possible a fast tuning of the beams and optimisation of the luminosity conditions.

Moreover, both PD and ET are of great importance for physics analyses: the ET to tag photo-production processes in a wide range of photon-proton centre of mass energy $W_{\gamma\mathrm{p}} = 80 \to 280\,\mathrm{GeV}$, the PD to measure initial state radiation processes (ISR) in deep inelastic scattering, eventually allowing F_L to be measured [4].

The HERA Luminosity Upgrade [5], the installation and first operation of which is scheduled for 2000, will provide a fivefold increase of the instantaneous luminosity, as compared to the original HERA design, to a peak value of $L \simeq 7.4 \cdot 10^{31}\,\mathrm{cm}^{-2}\mathrm{s}^{-1}$ and will include the longitudinal polarisation of the electron beam at the interaction point.

These planned HERA upgrades combined with the modifications scheduled for the beam lines near H1, in particular: *i)* a stronger bending (i.e. smaller bending radius) close to the interaction point which increases dramatically the intensity of synchrotron radiation incident on the PD and *ii)* the rearrangement of the position of many magnets in the tunnel, require a major upgrade of the present H1 luminosity system, mainly:

1. *for the Photon Detector*: in the new conditions the synchrotron radiation will be stronger ($\times 5$) and harder (critical energy up to 160 keV for 30 GeV electrons); for the 5 year running period of HERA after the year 2000, the doses deposited by the BH photons is a contribution which cannot be neglected ($\sim 25\,\mathrm{Mrad/year}$). Since the present calorimeter made of KRS (KRistallSchmelze) crystals already suffers from radiation damage under a present annual dose of $\sim 8\,\mathrm{Mrad}$ a completely new technique based on quartz-fibre, with an energy and (x, y) impact position resolution of $\sim 20\,\%/\sqrt{E/\,\mathrm{GeV}}$ and a few mm respectively, is proposed (section 3);

2. *for the Electron Tagger*: due to the small available space in the 2000 beam line setup, a new compact Electron Tagger (Tungsten/Sci-Fibre) has to be build (section 4);

3. *for the Electronics:* at nominal luminosity one expects at least one photon per bunch crossing in the PD. The linearity of the photomultiplier response and a complete removal of bunch to bunch pile-up are crucial to get unbiased total energy distributions. The present electronics and pulse transmission do not fulfil these stronger requirements. A solution based on analog processing with a 40 MHz rate sampling 12 bit ADC is proposed (section 5);

4. *for the dedicated Luminosity DAQ,*: online high statistics histograms of all relevant quantities ($E_{\mathrm{tot.}}$ for each bunch, (x, y) impact points, ...) are required for an accurate

control of the system and for the bunch by bunch luminosity measurement once per minute with an accuracy of 1 %. The latter is related with the HERA polarisation measurement [6] and a non-negligible spread of the bunch luminosities at HERA (typically $\pm 10\%$ around the average value of $\langle L_{\mathrm{b}} \rangle$) is expected. Such a measurement cannot be performed by the present acquisition with the needed precision. A foreseen solution based on PowerPC processors is described in section 5.

In the next section the methods of the luminosity measurement are outlined. The design of the new Photon Detector and the Electron Taggers, based on the SpaCal technique is described in sections 3 and 4. Solutions for the electronics and the data acquisition are presented in section 5. Section 6 briefly describes the detector calibration and the monitoring of the system. The final section summarises the project funding and the time scale for its realisation.

2 The Method

For the head-on collisions, the *per bunch* instantaneous luminosity L_{b} is related to the bunch parameters via

$$L_{\mathrm{b}} = \frac{N_{\mathrm{e}} N_{\mathrm{p}} f_0}{2\pi \sqrt{\sigma_{\mathrm{e},x}^2 + \sigma_{\mathrm{p},x}^2} \sqrt{\sigma_{\mathrm{e},y}^2 + \sigma_{\mathrm{p},y}^2}} \tag{2}$$

where f_0 is the bunch revolution frequency, N_{e} and N_{p} are the number of electrons and protons in the bunch and σ_x, σ_y are the transverse dimensions of the lepton and proton beams at the interaction point. The integrated luminosity $\mathcal{L}_{\mathrm{b}}$ within a given time interval ΔT is given by:

$$\mathcal{L}_{\mathrm{b}} = \int_0^{\Delta T} L_{\mathrm{b}}(t) \mathrm{d}t \tag{3}$$

The total integrated luminosity $\mathcal{L}$ is the sum over all colliding bunch crossings: $\mathcal{L} = \sum_{i=1}^{n_{\mathrm{ep}}} \mathcal{L}_{\mathrm{b}}^i$.

Using reaction (1) the integrated luminosity can be determined from the number of produced photons above a given energy threshold:

$$N_\gamma(E > \epsilon) = \mathcal{L}_{\mathrm{b}} A \int_\epsilon^\infty \frac{\mathrm{d}\sigma_{\mathrm{BH}}}{\mathrm{d}E} \mathrm{d}E \tag{4}$$

where $\mathrm{d}\sigma_{\mathrm{BH}}/\mathrm{d}E$ is the differential cross-section of the Bethe-Heitler reaction [7] and A denotes the geometrical acceptance for detection of BH photons. The number of produced photons per bunch crossing within the acceptance of the detecting system follows Poissonian statistics $P(k;\mu)$ with a mean value of

$$\mu \equiv \langle N_\gamma \rangle = N_\gamma / (f_0 \Delta T) \tag{5}$$

A typical distribution of the total energy deposited in the Photon Detector is shown in fig. 1. The shape of this distribution is governed by the luminosity dependent average number of photons $\mu(L_{\mathrm{b}})$, energy resolution $\sigma(E)$, minimum energy cutoff ϵ of the detector and the amount of e-gas background. Note, that although the background can be controlled using electron pilot bunches, a simple subtraction procedure for differential energy distributions is only approximately valid at relatively low luminosity, when $\mu << 1$. Neglecting here for simplicity the problem with background, the total measured energy spectrum in the PD is described by a superposition of events with different photon multiplicity:

$$\frac{\mathrm{d}N}{\mathrm{d}E_{\mathrm{PD}}} = \sum_{k=0}^{\infty} P(k;\mu) \int f_k(E = E_1 + \cdots + E_k) \cdot G(E_{\mathrm{PD}}; E, \sigma(E)) \mathrm{d}E \tag{6}$$

where $f_k(E)$ is the energy distribution of k overlapping BH photons and $G(E_{\mathrm{PD}}; E, \sigma(E))$ represents a Gaussian smearing due to finite energy resolution of the Photon Detector. In practice, at design peak luminosity up to 10 terms in (6) have to be taken into account.

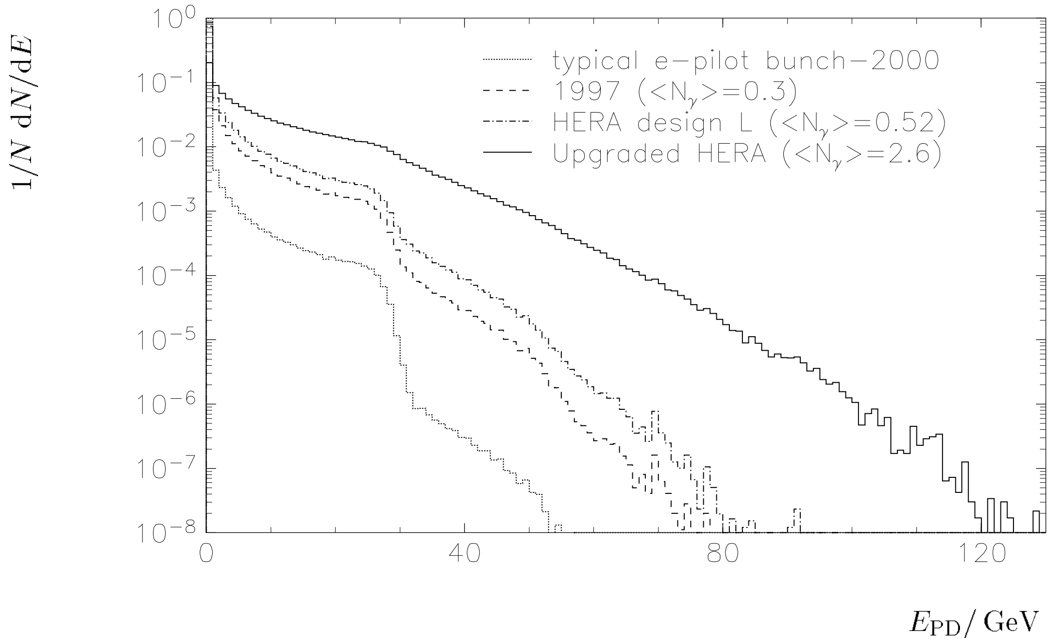

Figure 1: Distribution of the total energy deposited in the Photon Detector for different luminosities and for lepton beam energy 27.6 GeV. The calorimeter cutoff ϵ was set to 130 MeV, corresponding to $\sim 2\,\mathrm{X}_0$ filter in front of the PD, and the energy resolution of $25\,\%/\sqrt{E}$ was assumed.

The most precise procedure for the luminosity determination is based on a complete analysis of the photon energy spectrum $\mathrm{d}N_\gamma/\mathrm{d}E$. In practice the smeared $\int f_k G \mathrm{d}E$ are easily obtained for all contributing k by convoluting a measured low L_b sample ($\simeq f_1$) with itself $k-1$ times. The average number of photons per bunch crossing, μ, can then be fitted from (6), and finally $\mathcal{L}$ is determined using formulae (4,5). Preliminary results from a simple simulation with an energy resolution of $20\,\%/\sqrt{E/\,\mathrm{GeV}}$ show that μ can be fitted with an accuracy of $0.2\,\%$ in the expected luminosity range. The contributions of the various systematic effects to the accuracy are under investigation.

In addition to this method, two simpler solutions are proposed for the on-line ($\sim 1\,$Hz) luminosity measurement, supplemented by the regular analysis of the $E_{\rm tot.}$ distribution to control the photon energy scale and to calculate all necessary corrections.

The first one, called "simple counting method" and now in use in the present system, is based on the dead-time-free counting of the bunch crossings with energy deposit above a certain trigger threshold, $N_{\rm BC}(E > E_{\rm thr.})$. It has to cope with the in-bunch pile-up photons unresolvable in the calorimeter. This leads to the following two main effects: *i)* two (or more) photons each with an energy above $E_{\rm thr.}$ give one count in place of two (or more), *ii)* two (or more) photons with an energy below $E_{\rm thr.}$, but having total deposit $E_{\rm tot.} > E_{\rm thr.}$ give one spurious count. For every value of luminosity L, there exists an energy $E_{\rm thr.}(L)$ for which an exact compensation is fulfilled, i.e. $\langle N_\gamma(E > E_{\rm thr.})\rangle = \langle N_{BC}(E > E_{\rm thr.})\rangle$. This value of $E_{\rm thr.}$ slowly varies from $\sim 5\,$GeV at $L = 1\ \mu\mathrm{b}^{-1}\mathrm{s}^{-1}$ to $\sim 7.5\,$GeV at $L = 75\ \mu\mathrm{b}^{-1}\mathrm{s}^{-1}$. Fig. 2 shows that $E_{\rm thr.} = 7\,$GeV could be an optimal choice of the trigger threshold, for minimising the pile-up correction for the simple bunch counting method:

$$|\delta_{N\gamma}| < 2\,\%, \quad \text{for} \quad L = 15 \rightarrow 75\ \mu\mathrm{b}^{-1}\mathrm{s}^{-1},$$

covering full range of luminosities after HERA upgrade. At this value of threshold, a $1\,\%$ systematic error in the absolute energy scale translates into $0.6\,\%$ uncertainty in the integrated

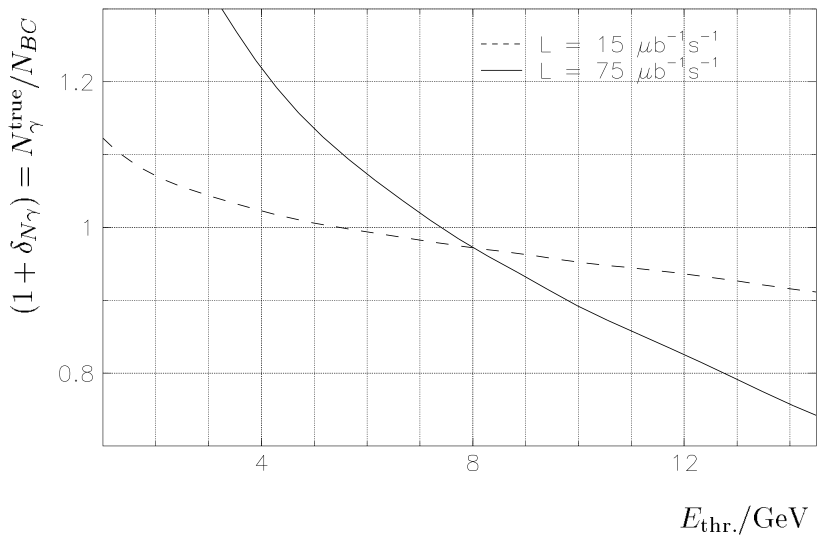

Figure 2: Pile-up correction to the photon rate method as a function of the trigger threshold for two extreme running conditions of the upgraded HERA.

luminosity $\mathcal{L}$. Hence one needs to control the online E-scale at $\sim 1.5\%$ level. The sharpness of the trigger threshold is not so critical, and the variations of $\sigma(E_{\rm thr.})$ between 0.2 and 1.2 GeV contributes less than 0.2% to the $\delta\mathcal{L}$.

Another possibility [8] to determine luminosity, which is especially suited for high intensity environment, is to measure the total energy flux of BH photons in the Photon Detector:

$$E_{\rm ep} = E_{\rm tot} - E_{\rm bgr} = \mathcal{L} A \int_\epsilon^\infty E \frac{{\rm d}\sigma_{\rm BH}}{{\rm d}E} {\rm d}E \tag{7}$$

where $E_{\rm tot}$ is the total measured energy in the given time interval, while $E_{\rm bgr}$ is the background energy which can be measured using electron pilot bunches. This method automatically accounts for in-bunch pile-up. Also the background subtraction procedure in this case works correctly at any value of luminosity. Comparing the equations (4) and (7) one gets

$$\mathcal{L} = \frac{N_\gamma(E>\epsilon)}{A\sigma_{\rm BH}(E>\epsilon)} = \frac{E_{\rm ep}}{A\sigma_{\rm BH}(E>\epsilon)\langle E_{\rm BH}\rangle}$$

where $\langle E_{\rm BH}\rangle$ is the average photon energy created in the process (1). The accuracy of this method has to be studied with respect to the different systematics errors.

The main contributions to systematic error $\delta\mathcal{L}$ are summarised in Table 1. The improvements are essentially due to "online" control of the systematic effects through the increase of computing power, allowing the movement of corrections from "off-line" to "on-line", the effect of which can be appreciated in the fig. 3 for the '97 running period. Two points are briefly discussed, the theoretical uncertainty and the acceptance correction.

Since the unbiased energy distribution is an essential requirement in the methods which automatically and correctly treat in-bunch pile-up, the data for those methods should be collected by an energy independent sampling. This imposes the requirement of a precise measurement of the cross-section at low E_γ. While the Landau-Pomeranchuk-Migdal suppression [9, 10] is not expected to be visible at HERA [11], the effect of the finite transverse beam size [12] becomes important, as has been measured recently [13]. As an example, fig. 4 illustrates a correction to the BH cross-section taking into account the real transverse dimensions of electron and proton bunches at HERA. One can see that the correction becomes as

Table 1: A break down of the H1 integrated luminosity systematic effects, $\delta\mathcal{L}$ (%)

Item	Online Actual	Offline Actual	Online Upgrade
Theoretical uncertainty	0.5	0.5	0.5
Trigger efficiency	0.1	0.1	–
Background subtraction	0.3	0.2	0.2
Pile up corrections	0.3	0.2	–
Photon detector acceptance	1.0	0.6	0.5
E-scale, resolution	2.0	0.7 – 1.2	0.6
p-bunch satellites	2.0	0.5 – 1.0	

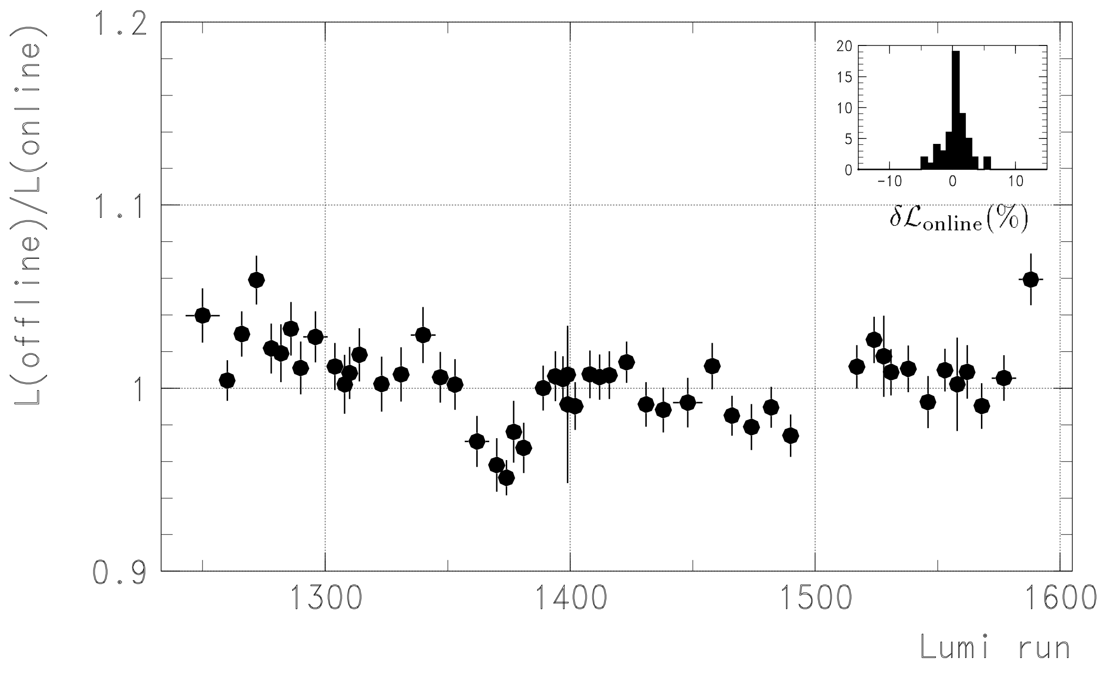

Figure 3: Off-line corrections to the on-line luminosity measurements in the year 1997. The insert in the upper right corner shows the distribution of the total systematic error of the online luminosity measurements in various lumi fills.

large as $3-4\%$ for the total photon yield above $E_{\rm thr.} = 0.1 \rightarrow 1\,\mathrm{GeV}$ and it may vary by $\sim 10\,\%$ for different beam optics.

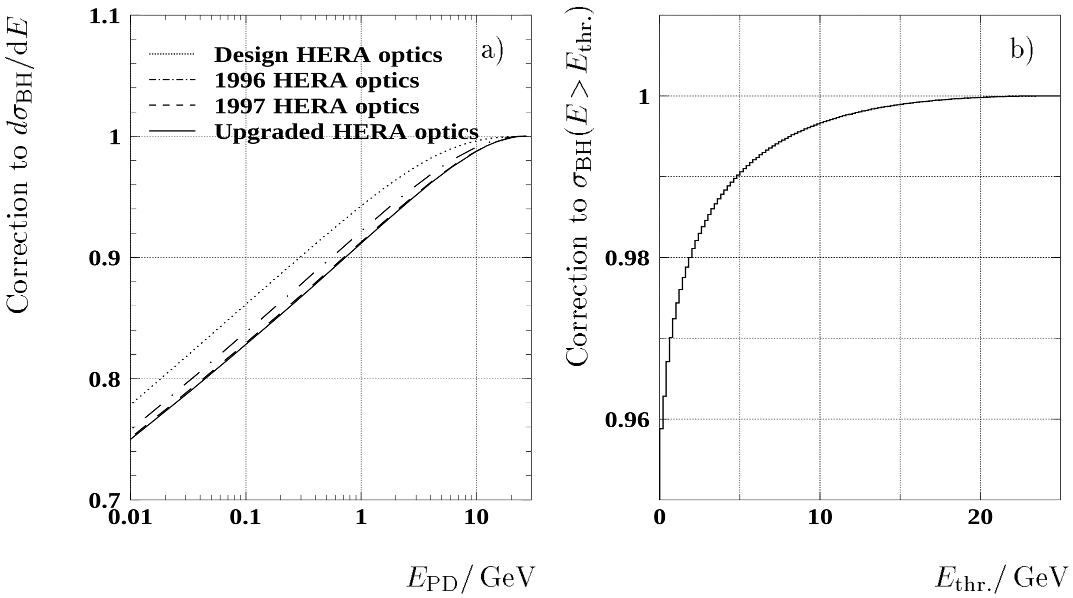

Figure 4: Beam size correction: a) to the differential BH cross-section for different optics parameters, b) to the total energy spectrum above a given threshold for the upgraded HERA optics.

The geometrical acceptance A of the Photon Detector is an important parameter which is controlled by the 2-dimensional coordinate distribution of the photon impact points. It can be determined directly from the data by fitting a Gaussian $G(x,y)$ shape in the central part of the detector with $100\,\%$ acceptance and extrapolating to the tails. As cross check, a Monte Carlo (MC) simulation can be used to calculate the acceptance value as a function of the lepton beam parameters: $A(\theta_x, \theta_y, x_{\rm off}, y_{\rm off})$. An example of such a procedure (using present HERA data) is illustrated in fig. 5.

It is important to remark that the correction due to non Gaussian tails of the proton bunches — so called satellite correction [14] — cannot be made by the luminosity system itself; the longitudinal structure of the proton bunches is measured by the additional proton pick-up device (PPU) and can also be controlled by the H1 time-of-flight system (TOF).

3 Photon Detector

The Photon Detector is an electromagnetic calorimeter of transverse size $\approx 12\times12\,\mathrm{cm}^2$ and covers, for the luminosity measurement, the full size of the γ beam ($\sigma_x\times\sigma_y \sim 2\times1.5\,\mathrm{cm}^2$, given by the divergence of the electron beam). This calorimeter has to be: *i)* protected from the synchrotron radiation by a shielding of minimum (in terms of X_0) thickness, *ii)* radiation resistant with respect to the total dose deposited by the Bethe-Heitler photons and residual synchrotron radiation. Dose calculations are detailed in the next subsection. The proposed calorimeter, a Čerenkov SpaCal, is shown schematically in fig. 6.

The Photon Detector is made of quartz-fibre planes between absorber plates, and is longitudinally segmented into two parts, a presampler about $4\,\mathrm{X}_0$ thick and a main calorimeter of sufficient depth (about $25\,\mathrm{X}_0$) to fully contain the electromagnetic shower. The presampler uses fibres that are more radiation resistant and has finer strip granularity in the central part. Its absorber plates are made of tungsten for compactness of the showers.

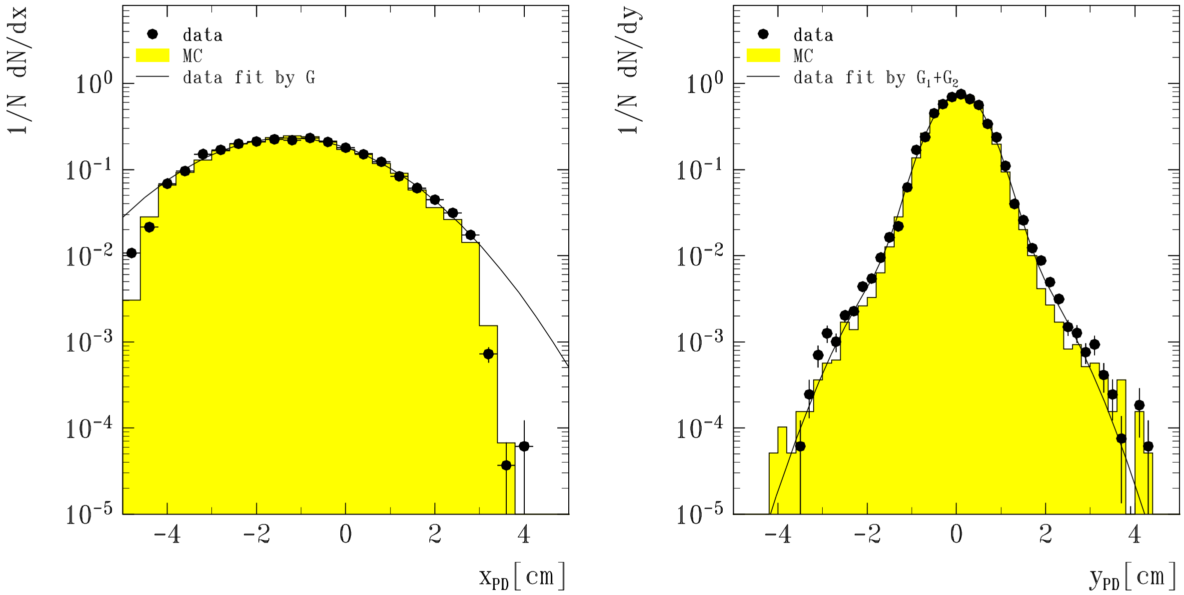

Figure 5: The coordinate distributions of photons at the PD for present HERA conditions. The $\sigma_{y,\mathrm{PD}}$ will be increased by a factor ~ 2 at the upgraded HERA.

With this configuration, the energy resolution is not deteriorated by the $> 4\,\mathrm{X}_0$ of inactive shielding, which would be needed to protect the present calorimeter; a Bethe-Heitler γ converting at the entrance of the PD is fully sampled. On the other hand, the synchrotron radiation is not expected *a priori* to produce significant background inside the quartz-fibres; this has to be confirmed by a detailed simulation.

3.1 Radiation Doses

The Photon Detector is exposed to several sources of radiation: bremsstrahlung photons, synchrotron radiation, and beam halo. The radiation dose from the latter has to be extrapolated from dosimetric measurements performed near the present Photon Detector.

The energy deposition of the former two in the volume of the detector is very different, owing to the different energy ranges. The bremsstrahlung photons deposit their energy almost uniformly over the shower length, whereas the high energy tail of the synchrotron radiation ($\sim 500\,\mathrm{keV}$ to $2\,\mathrm{MeV}$), which is not rapidly absorbed, is responsible for strong irradiation of the first layers of the detector.

Bremsstrahlung photons

The total bremsstrahlung cross-section for photons above 10 MeV is 0.5 barn with a mean photon energy of $\sim 2.5\,\mathrm{GeV}$. For an annual integrated luminosity of $200\,\mathrm{pb}^{-1}$ this leads to an annual energy deposit of 37 kJ in the calorimeter.

The fraction of this energy that is absorbed by the sampling material depends on the ratio of absorber and sampling material and their respective values of $(\mathrm{d}E/\mathrm{d}x)_{\mathrm{min}}$. It can vary between 2.3 % for a 4:1 tungsten/scintillator calorimeter to 12.8 % for a 2:1 lead/quartz calorimeter. For a 2:1 tungsten/quartz fibre calorimeter this fraction is about 8 %.

Assuming that 68 % of the energy are deposited uniformly in a cylinder of 2 cm radius and length $10\,\mathrm{X}_0$ we arrive at a total annual dose of 2 Mrad for the central part of a 2:1 tungsten/quartz fibre calorimeter.

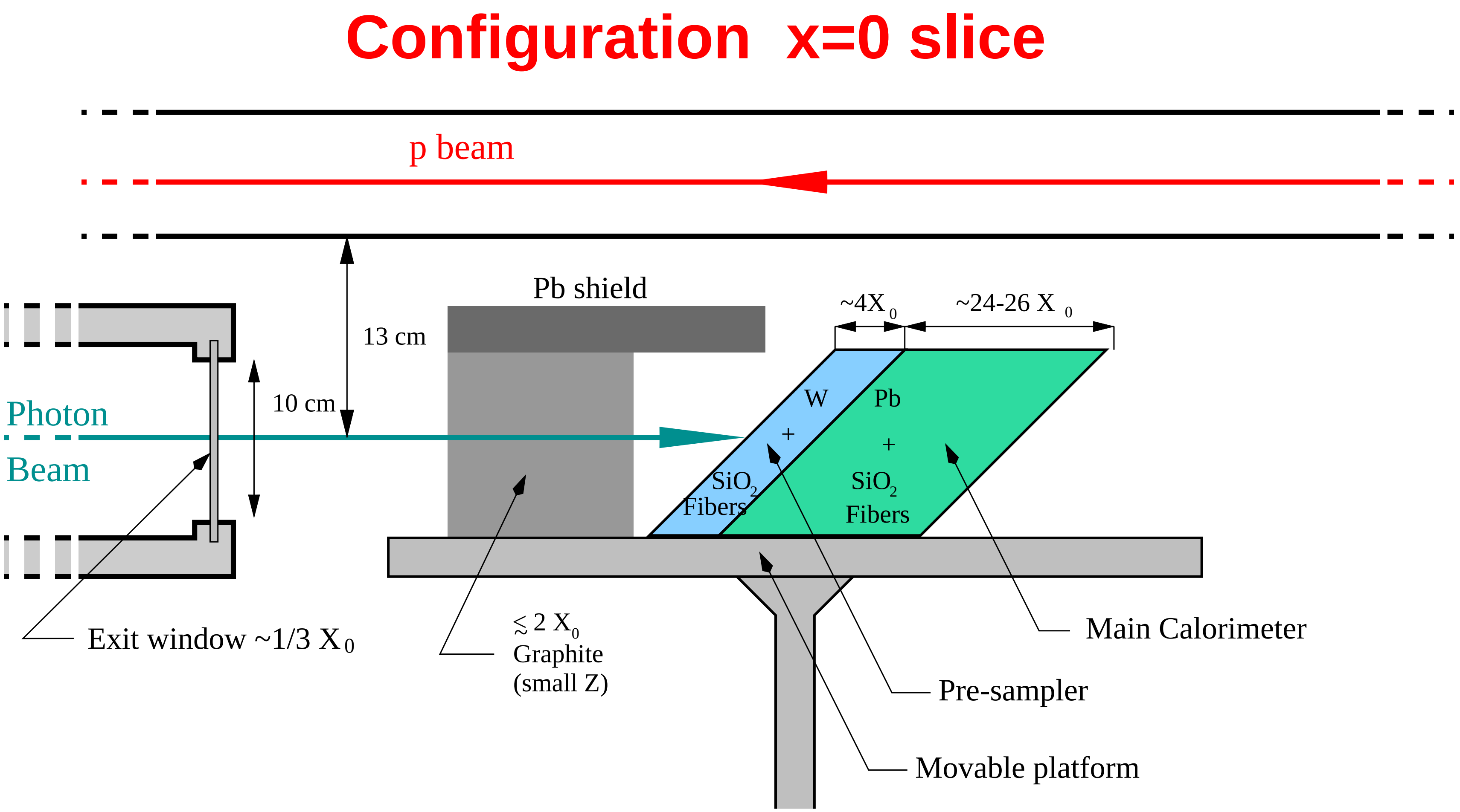

Figure 6: Layout of the detector in the tunnel: the γ beam axis is 13 cm below the proton beam pipe. An absorber of roughly $2\,X_0$ reduces the amount of synchrotron radiation (and the produced heat) directly hitting the presampler and the main calorimeter. All the detectors are mounted on a vertically movable table.

Synchrotron radiation

The following calculations are based on a critical energy of 160 keV and a total received power of 3.8 kW [15]. The SR photon spectrum for these parameters is shown in fig. 7. Also shown is the spectrum of the photons after 1, 2, 3 and 4 X_0 of carbon. Note that a substantial fraction of photons around 400 keV penetrate far into the detector, and causes radiation damage in the deeper layers.

Furthermore, photons above 1.2 MeV may create e^+e^- pairs with one particle above the Čerenkov threshold, which may constitute a source of background. The impact of this background depends on the exact form of the detector threshold which has to be determined by detailed simulation. However, this background will be insignificant if the threshold lies above ~ 3 MeV, due to the exponential drop-off of the synchrotron radiation spectrum (cf. fig. 7).

The energy absorption and the modification of the photon spectrum depends strongly on the material. This can be seen in fig. 8 where the total transmitted energy as a function of the traversed thickness measured in units of radiation length is shown. High Z materials are more efficient at absorbing low energy photons ($\lesssim 100$ keV), whereas materials with lower Z values suppress better the high energy tail of the synchrotron radiation spectrum.

The annual dose per incident power on the first layer of sampling material is about 3 Grad/W, assuming 10^7 s of beam per year, uniform distribution of the synchrotron radiation on a surface of $1\times10\,\mathrm{cm}^2$, and the energy-absorption coefficient of glass $\mu_{\mathrm{En}}/\rho = 0.028\,\mathrm{cm}^2/\,\mathrm{g}$ [16].

In order to achieve tolerable — even for quartz fibres — radiation levels, the power incident on the first layer of fibres has to be reduced below the 1 W level, by the appropriate combination of materials for the inactive shielding of minimum thickness. Low-Z materials may play a rôle here. The increase in total synchrotron radiation power calls for a detailed study of the temperature rise in the absorber. Water cooling of the inactive shielding will probably have to be considered.

3.2 Fibre choice

The total Čerenkov light yield depends on the fibre numerical aperture and on its spectral properties. The numerical aperture of a fibre is defined as $\mathsf{NA} = n_{\mathrm{core}} \sin\theta$ where n_{core} is the refraction index of the fibre core and θ is the maximum angle of a median ray with respect to the fibre axis that is propagated by total internal reflection, and thus has the value $\mathsf{NA} = \sqrt{n^2_{\mathrm{core}} - n^2_{\mathrm{clad.}}}$. The higher NA, the larger is the part of the Čerenkov cone that is propagated by the fibre.

Two types of fibres have been used in previous quartz fibre calorimeters, fluorine-doped silica clad and polymer clad fibres. In both cases the core is made of high-purity fused silica, with high hydroxyl content to increase radiation resistance.

Polymer clad fibres have a higher numerical aperture than silica clad fibres (0.37 vs. 0.22). However, the former possess a higher cut-off wavelength (due to the absorption of the evanescent wave in the cladding) whereas silica clad fibres transmit well down to 250 nm.

Simulations and direct measurements have shown [17] that for the Čerenkov spectrum the gain by the increased spectral reach of silica clad fibres is cancelled by their lower numerical aperture, leading to roughly the same light yield for these two fibre types.

Polymer clad fibres are several times less expensive than silica clad fibres; they are also easier to handle and less prone to break. Therefore, they can be used without a supplementary coating, minimising inactive space between adjacent fibres in a calorimeter plane, whereas silica-clad fibres have to be protected by a coating. However, in terms of radiation hardness, polymer clad are worse: they lose about 50 % transmittance after having received an irradiation dose of 1 Grad, whereas silica clad fibres only lose 10 % [17].

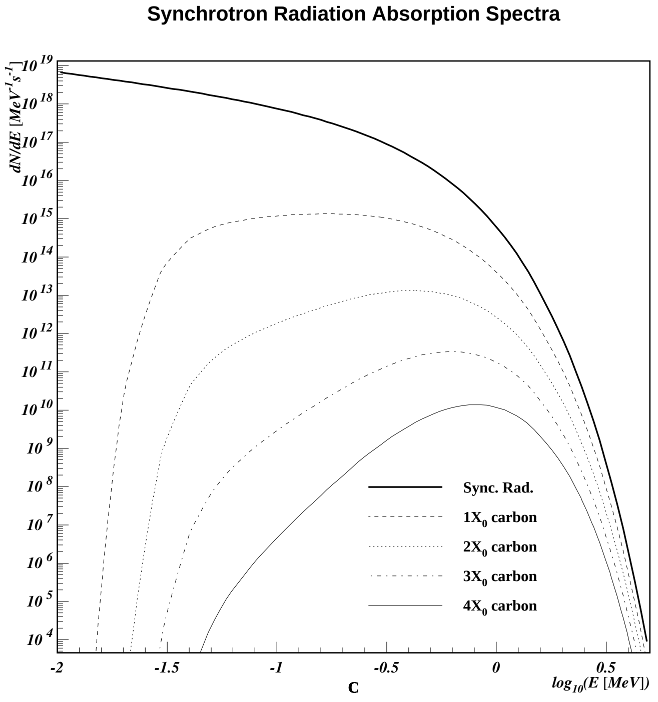

Figure 7: Synchrotron radiation energy spectrum for $E_{\mathrm{crit.}} = 160\mathrm{keV}$ and $P_{\mathrm{tot.}} = 3.8\,\mathrm{kW}$ and spectrum of transmitted photons after carbon absorbers of various thicknesses.

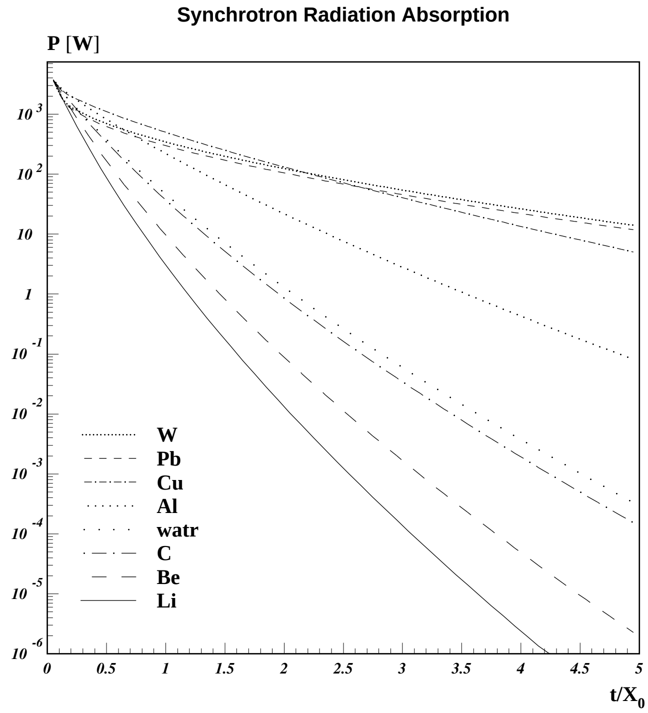

Figure 8: Energy attenuation of synchrotron radiation as a function of traversed thickness in units of radiation length for various materials ($E_{\mathrm{crit.}} = 160\mathrm{keV}$ and $P_{\mathrm{tot.}} = 3.8\mathrm{kW}$).

3.3 Presampler

The Čerenkov fibre SpaCal [17, 18] technique has a major difference compared to the one using scintillating fibres: the produced Čerenkov light inside the fibre is collected when the fibre axis is oriented at 45° (±5°) relative to the incident particles; the width of 5° depends on the numerical aperture of the fibres [17]. The typical yield is $\sim$ 0.8-1 photo-electron per mm of fibre.

This implies to arrange the fibres in a plane tilted with respect to the plane perpendicular to the beam direction z. However it is still possible to have independent x and y coordinates measurements (i.e. perpendicular when seen along the z axis) by choosing appropriately the tilt of the front plane of the calorimeter and the orientation of the fibres in that plane (see fig. 9).

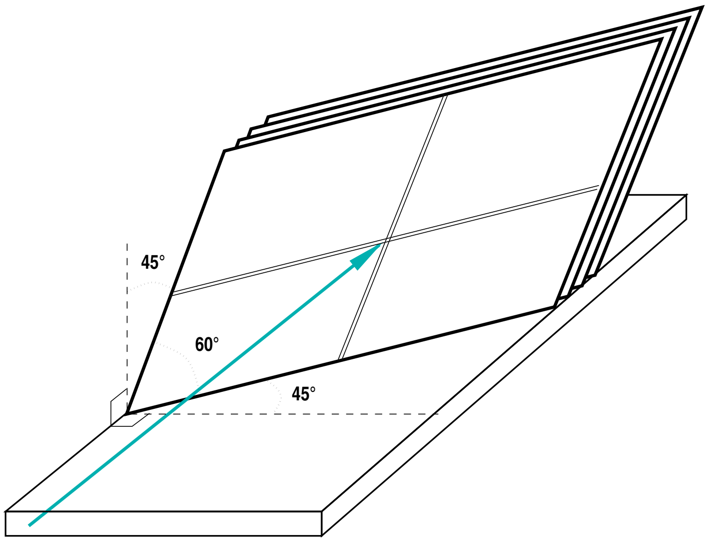

Figure 9: Placement of the fibres in the calorimeter sampling planes ensuring independent (x, y) impact position measurement.

For both coordinates, the fibres can be connected to n readout devices, each channel corresponding to a band of a given width (2 cm with $n = 6$ for instance), summed over the depth of the presampler. If necessary, a finer granularity can be designed in the central region without increasing significantly the number of readout channels (see fig. 10); this finer granularity (1 cm for instance) allows the measurement of the γ beam (x, y) position distribution and to tag two photons versus one for radiative events.

The presampler is expected to reduce the synchrotron radiation to a level where the use of polymer clad quartz fibres can be envisaged for the calorimeter, drastically reducing the cost of the fibres. The exact parameters of the presampler have still to be optimised in detailed simulation; a depth of 4 X_0 and 16 channels (8 for each side) will be used as a starting point.

3.4 Main calorimeter

Adjoining the presampler, we consider a main calorimeter based on the same geometrical arrangement. Again, tungsten absorber plates are preferred due to the smaller Molière radius which can be achieved ($\sim$ 1.3 cm for a 2 : 1 W:fibre ratio). Lead absorber plates are a cheaper alternative, if a higher Molière radius can be tolerated.

Compared to a more conventional geometry (horizontal towers), it has the advantage of providing an easy way to feed the calibration light into the fibres by their free end without introducing additional devices.

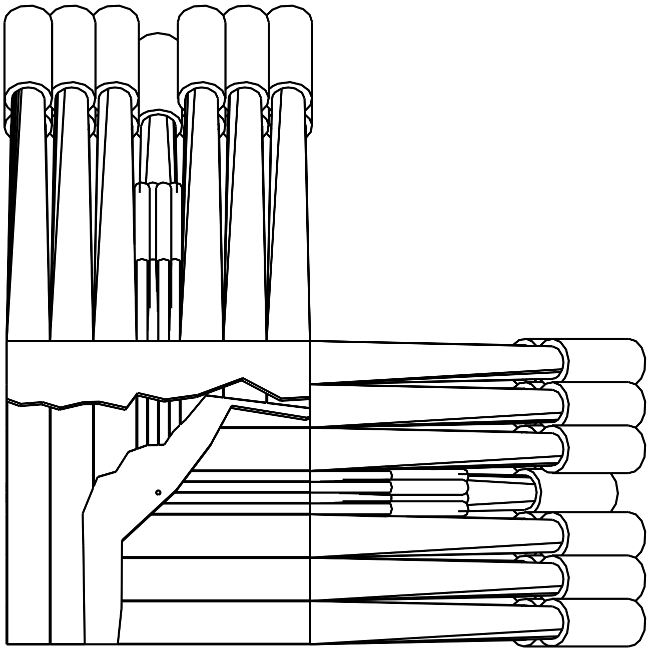

Figure 10: Front view of the of the presampler. Each slice in x and y corresponds to a different channel, with a finer granularity in the central region.

The position measurement is done in the same way as for the presampler with the $\sim 25\,\mathrm{X}_0$ depth being integrated in the same readout strip channel. A finer spatial resolution in the central region would not be needed here; assuming the same granularity as in the presampler, the calorimeter has 12 separated channels (6 for each side), leading to a total number of 28 channels, for the presampler and the main calorimeter.

Quartz-fibre calorimeters have achieved energy resolutions of $\sim 25\,\%/\sqrt{E} + 3\,\%$ [17] for a lead:fibre volume ratio of 4:1. Due to the numerical aperture of the fibres, the photostatistic contributed in this case to half of the stochastic term. Lowering the sampling ratio reduces the stochastic term by increasing the photostatistic and by reducing sampling fluctuations. The optimisation of the energy resolution part originating from the sampling fraction term will be investigated by detailed simulations and measured on prototypes. Furthermore, it has been shown [17] that the constant term can be made to vanish by arranging fibres in planes instead of the staggered geometry used in the above-mentioned prototype.

4 Electron taggers

The luminosity increase in the upgraded HERA is achieved by an earlier separation of the e and p beams. For this purpose the HERA magnet elements close to H1 are moved, which means that the Electron Tagger positions must be newly adjusted. The determination of optimal positions for the taggers and the study of their acceptances has been performed using the fast Monte Carlo (MC) simulation package H1LUMI [19] upgraded to take into account the future beam optics.

The present status of the new magnet layout near the IP is given in fig. 11. Electron tracing made according to this layout shows (fig. 12) that it is reasonable to place taggers between the end of the cold magnet BG and the horizontal focusing quadrupole QI2. The requirement of compactness is absolutely essential for these taggers.

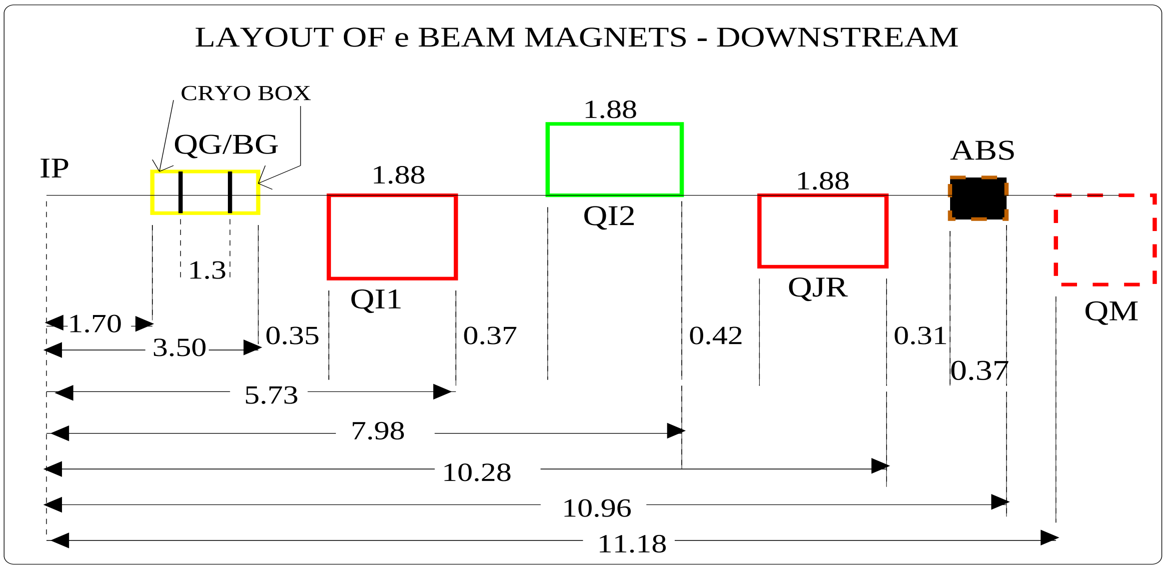

Figure 11: Upgraded HERA magnet layout near the IP (distances are in m).

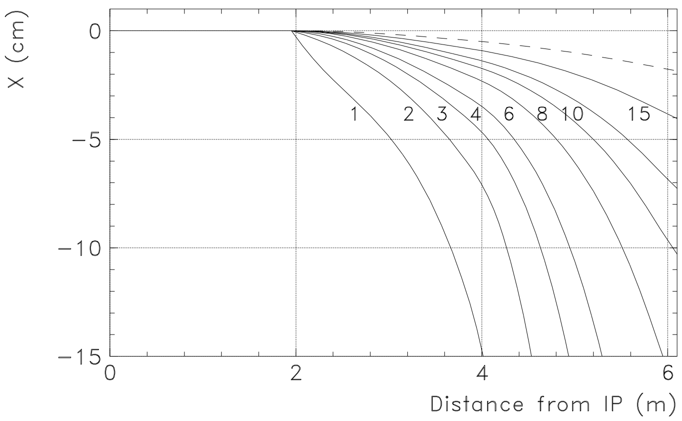

Figure 12: The trajectories of electrons with energies from 1 GeV to 27.5 GeV downstream of the IP (dashed curve corresponds to 27.5 GeV).

ET6

The only place for an electron calorimeter is the gap between magnets QI1 and QI2. As is seen in fig. 13 the accelerator beam pipe inside the quadrupole QI1 can be widened to allow for an exit window with a lateral length $\sim 8\,\mathrm{cm}$ for recoil electrons at the downstream edge of QI1 (5.7 m from IP). Behind the exit window it is planned to install the ET6: a Compact

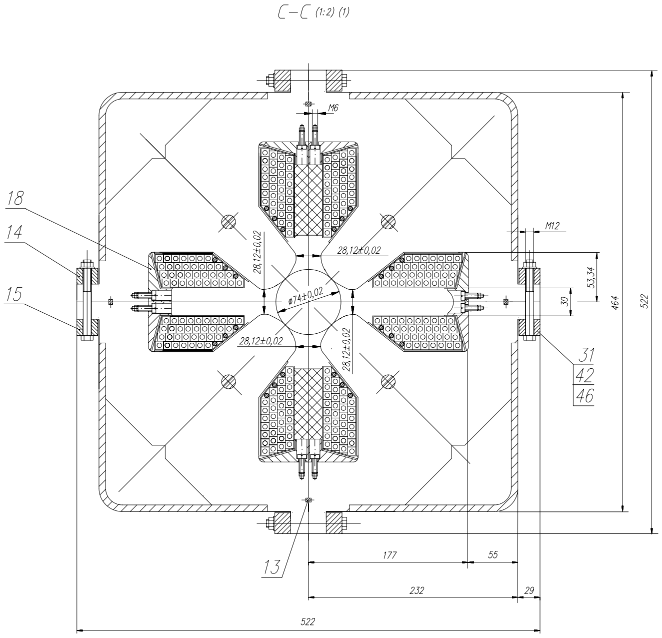

Figure 13: Cross section of QI1 quadrupole with the horizontal gap for the beam pipe.

Tungsten Calorimeter (CTC). CTC is a SpaCal type calorimeter, containing scintillating fibres of 0.5 mm in diameter with a filling coefficient of $\sim 25\,\%$ (W:Fibre ratio of 4:1). It is characterised by a small Molière radius of $\mathrm{R_M} \simeq 1\,\mathrm{cm}$ and $\mathrm{X_0} \simeq 0.7\,\mathrm{cm}$. An energy resolution better than $10\,\%/\sqrt{E/\,\mathrm{GeV}}$ is expected.

The MC simulation shows (fig. 14a) that recoil electrons stay within the vertical size of $y_{\mathrm{e}'} = \pm 1.5\,\mathrm{cm}$ from the e beam axis for ET6 position near the beam pipe of 4 cm radius. This gives the recommended thickness of 4 cm for CTC. Its optimal lateral length is determined by the $x_{\mathrm{e}'}/E_{\mathrm{e}'}$ correlation plot (fig. 14b) as 8 cm. The plot illustrates that the precise coordinate measurement is necessary for good energy reconstruction for those events which hit the detector near the boundary, where sizable leakage of the electromagnetic shower occurs.

Thus ET6 with a size of $4\times 8\times 15\,\mathrm{cm}^3$ will cover the whole available space and provide maximum possible acceptance for photo-production events. Good spatial resolution, allowing the determination of the electron impact point with precision $\sim 1\,\mathrm{mm}$, can be achieved with energy readout from different parts of the detector. As option a preshower made of CTC elements with vertical fibre alignment is also considered for improved space resolution. The readout will be performed using photomultipliers (PM). A light calibration system is also foreseen, to monitor the PM response and the light transmission in the fibres.

The energy distribution of electrons accepted by the CTC, given in fig. 14c, stems from the process of particle production by quasi-real photons with $Q^2 < 0.01\,\mathrm{GeV}^2$. The distribution covers an electron energy range from 6 to $11-14\,\mathrm{GeV}$, depending on the minimum distance of the CTC inner edge to the e beam axis. The ET6 acceptance distributions for these minimum distances are shown in fig. 14d. The corresponding energies of quasi-real photons will lie in the interval $11-20\,\mathrm{GeV}$, allowing the study of photo-production processes at $\langle W_{\gamma p}\rangle \sim 220\,\mathrm{GeV}$. Thus, after the HERA upgrade the ET6 will provide approximately the same conditions as

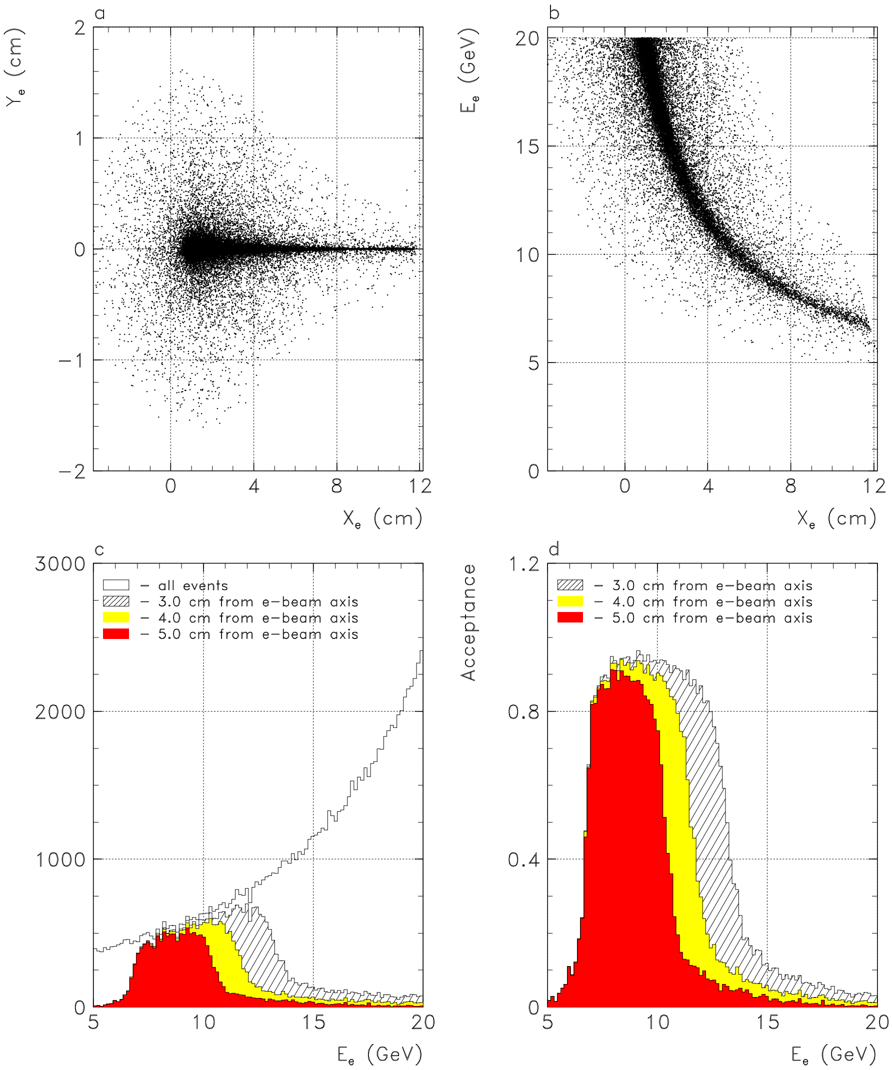

Figure 14: Scatter plot (a), correlation plot (b), events *vs* energy distribution of electrons (c) and acceptance (d) for ET6 .

the present ET33.

ET44

Since the future HERA magnet system stays almost unchanged at distances > 30 m from IP the tagger ET44 can be effectively used also after the HERA upgrade. The constituent KRS crystals have been replaced by NBW ($NaBi(WO_4)_2$) crystals for the 1998-1999 run period. The use of scintillating PWO ($PbWO_4$) crystals in ET44 to have better energy resolution (this is important for more precise acceptance determination) is under discussion. MC simulation performed for the new magnet lattice predicts approximately the same ET44 acceptance (fig. 15) as for the present HERA layout [20].

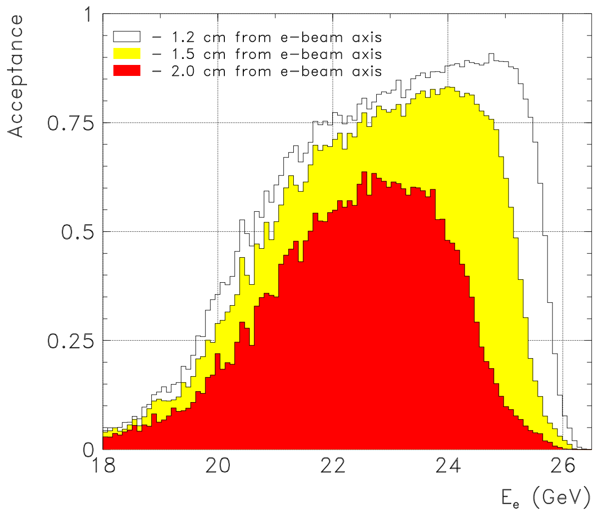

Figure 15: The results of acceptance simulation for ET44 for different positions of taggers relative to the e-beam axis.

Table 2 summarises the visible photo-production cross-sections in both Electron Taggers as function of their distances from the electron beam axis.

d(cm)	ET6	d(cm)	ET44
3.0	0.898 μb	1.2	5.17 μb
4.0	0.615 μb	1.5	3.90 μb
5.0	0.420 μb	2.0	2.19 μb

Table 2: Visible photo-production cross sections for electron taggers placed at different distances (d) from the electron beam axis.

The ability to require a detected electron/positron in the final state of high ET jet production and heavy flavour production will be important both in defining efficient triggering and for the best possible kinematic reconstruction of such processes.

5 Electronics

The general electronics layout is shown in fig. 16. This scheme is designed for both photon and electron detectors. It would also be a suitable solution for the upgrade of the polarimeter readout.

Basically, the calorimetric chain consists of a fast analog shaping, a 12 bit ADC providing 4 energy samples per bunch and a dedicated fast readout by a commercial processor (Power PC) which performs on-line histogramming at a high rate (~ 1 MHz). The analysis of the

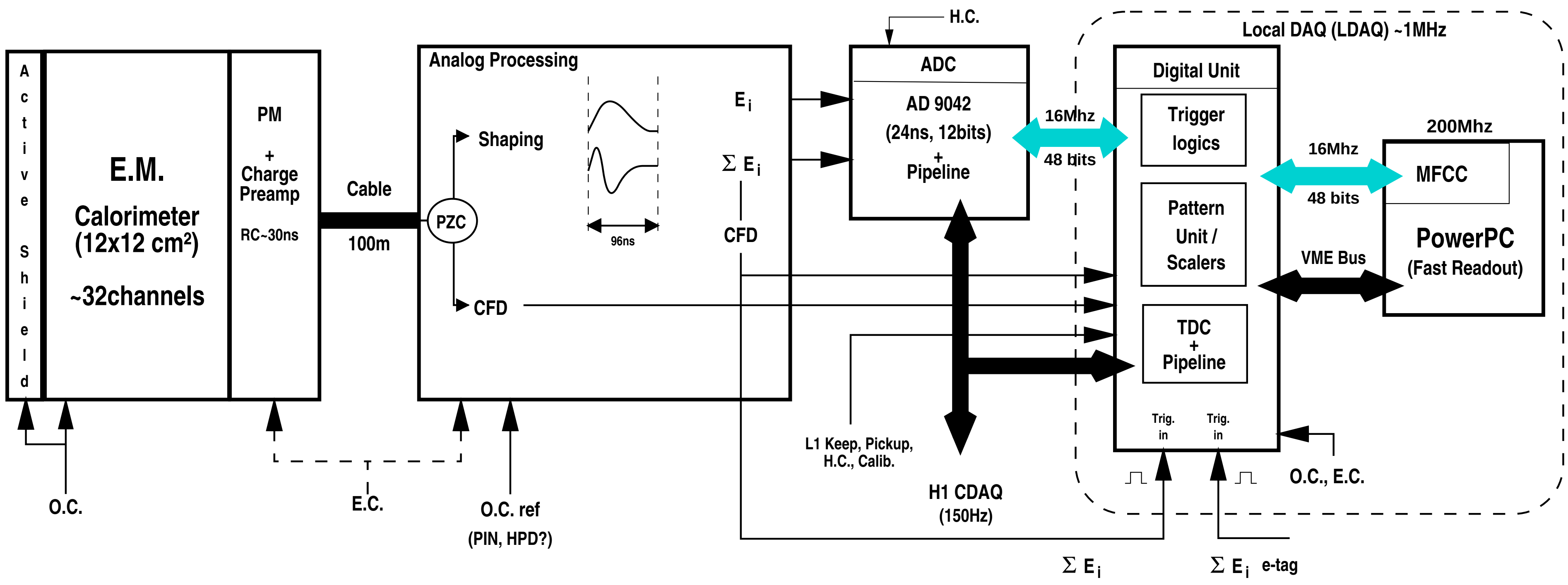

O.C. = Optical Calibration
E.C. = Electronics Calibration

Figure 16: Electronics scheme for the Luminometer

produced histograms provides the luminosity and polarisation measurements bunch by bunch. We describe now successively the main features of the components of this electronics which can be considered as split into two parts; photo-multipliers, preamplifiers $E_{\mathrm{tot.}}$ analog sum and electronics calibration pulsers at the detector level, the remaining part being located into a single rack installed in the North Hall, near the exit of the HERA tunnel.

5.1 Photodetectors

A 10 Mhz counting rate can be achieved by photomultipliers with the required linearity ($\sim 1\,\%$).

The present photomultipliers can in principle be re-used with an optimised voltage divider to cope with the higher counting rate. An alternative solution is to reduce the gain of the last stages of the PM and to perform a charge preamplification at the output of the PM. This solution has been worked out for the H1 SpaCal backward calorimeters without adding a significant noise contribution.

The definitive choice of the PM will depend on the photocathode area needed to fit the bundle size of the fibres.

5.2 The analog processing and digitization

- *Preamplification:* A first amplification can be performed at the detector level by a charge preamplifier. A typical 4 V output amplitude with a rise time of a few nanoseconds and a decay time $R_f C_f \sim 30$ ns is needed. A standard noise contribution ENC$\sim 3 \cdot 10^3$ electrons is expected, contributing only to an equivalent noise level of less than a photo-electron.

- $E_{\mathrm{tot.}}$ *summation:* The total energy calculation is performed for both detectors (pre-sampler, main calorimeter) by an analog summation of all the preamplifier outputs on a dedicated board. This provides an easy way to get a fast digitized total energy histogrammed, and minimises coherent noise summation.

- *Shaping:* Basically, it corresponds to one electronic board of 16 channels. It is proposed first to remove the skewing effect of the cable at the receiving end by a suitable filtering. A fast shaping is then performed, (pole-zero compensation PZC + unipolar or bipolar shaping) with a return to the baseline at the level of 1 % within one HERA clock period (96 ns) such that bunch to bunch pile-up effects are removed.

  This board includes also few constant fraction discriminators (CFD), their output being on one hand used for the luminosity counting and, on the other hand, digitized in a TDC (see below) and/or used as input for triggering. It is not necessary to discriminate all the channels because detailed timing information per channel is not needed for offline analysis. The $E_{\mathrm{tot.}}$ pulse and 3 or 4 channels only could be discriminated. The discrimination of the few channels is interesting with respect to calibration procedures and also for non-calorimetric channels (background vetos, optical calibration for instance) which would be processed in the same way.

  Typically, three such boards would cover the needs of the photon and electron detectors and the associated veto counters.

- *Digitization*: The amplitude measurement is performed inside a dedicated board (16 channels) based on a fast ADC. For instance, the AD9042 (Analog Device) chip performs 12 bits conversion at a maximum rate of 41 MHz. For our application, running the device at this rate (4 times the HERA clock frequency) would fit perfectly our application. The digitized information is stored in parallel inside two pipelines, one for the H1 central DAQ readout, the second one for the fast online DAQ (LDAQ). For the $E_{\mathrm{tot.}}$ channels a faster sampling frequency is foreseen for monitoring purposes, by interleaving two such ADC's.

- *Digital Unit*: This unit would consist of a few boards which will allow to record various digital informations (16) and to perform triggering in test mode.

  - Scalers: They provide a dead time free counting for all the trigger information: $E_{\mathrm{tot.}}$ thresholds, HERA clock cycles, etc.
  - Timing: This is very useful for the tuning and monitoring of the sampling position of the ADC with respect to the peak value of the analog pulse. The main signals which could be measured permanently by the TDC are: the total energy $E_{\mathrm{tot.}}$ and the individual channels discriminated in the analog card, the HERA clock, the beam pickups, the L1keep. The TDC function is performed by a chip developed at Paris VI for the BaBar experiment. It provides a time resolution of 0.5 ns and a history over 20 microseconds. Digitized information can be stored in a external pipeline. The low cost of this device allows to foresee 2 of them per channel, one for the H1 CDAQ, the other one for the local one.
  - Pattern Unit: Digital informations as the bunch number, trigger status ($E_{\mathrm{tot.}}$ for photon and electron detectors, optical calibration ...) are stored and decoded by the local DAQ for selective histogramming.

  The main triggering functions of the Digital Unit in test and monitoring modes are to select:

  - Optical calibration signals
  - coincidences between the total energy of both the electron and photon taggers for energy calibration purposes.

  The possibility to include these triggering functions inside the front-end Field Programmable Gate Array (FPGA) chip of the Multi-Function Computer Core MFCC 8441 board (see below) is under investigation.

- *Local high rate DAQ:* The LDAQ consists of a VME PowerPC mother board equipped with an MFCC developed by the CES company (see fig. 17).

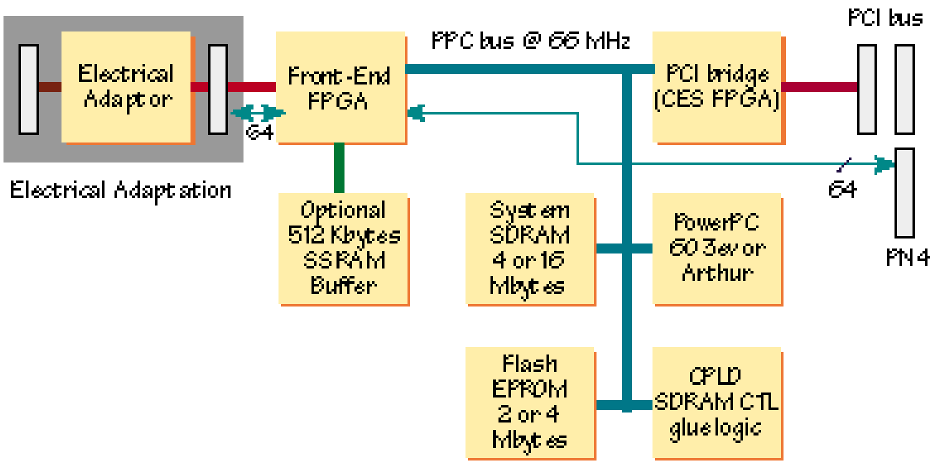

Figure 17: Layout of the MFCC board.

The high rate LDAQ readout is performed in two steps: first, the raw data (ADC, TDC, bits) are transferred via the 16 MHz, 48 bit bus (named MFCC bus) (see fig. 16) into the DRAM memory of the MFCC board. The PowerPC of this board performs the histograms and/or stores some raw events. Secondly, once per second the histograms/raw data and counters are transferred to the mother board card, on which energy/time scales, checks and luminosity calculations are done. A sketch of the VME luminosity crate is given in fig. 18 which shows the independent readout of the TDC and ADC boards by the MFCC and VME buses; PPC_1 and PPC_2 are respectively the PowerPC processor of the MFCC and VME mother boards.

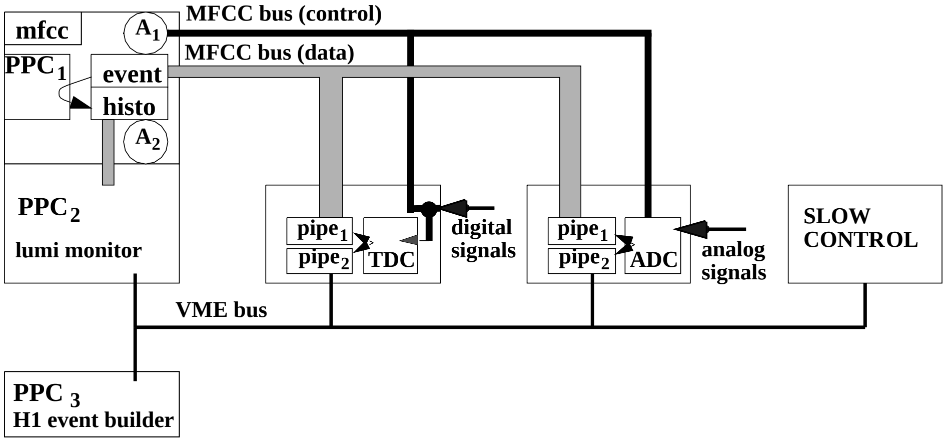

Figure 18: Scheme of the local high-rate DAQ

Typically, in a normal luminosity run, 220 bunches would be stored in the ADC/TDC pipelines and readout. The high rate histogramming would transfer only the 4 samples of each total energy (presampler, main calorimeter and E-tagger) in 3 cycles of the MFCC bus (180 ns). So the rate will be driven by the histogramming time of the PowerPC. x and y position measurements and other monitoring quantities will be histogrammed at a lower sampling rate (typically 10-20 kHz, according to the needs).

6 Calibration and Monitoring

The energy calibration and the monitoring of the Photon Detector and its electronics are important issues for $\mathcal{L}$ measurement. In this section we outline a possible procedure. It includes first the balancing of the channels of the calorimeter and the presampler, and secondly the absolute energy calibration.

Channel intercalibration:
Given the small sampling distance in units of X_0, the deposited energy distribution for vertical and horizontal strips have by construction the same value. Hence for a fixed vertical position of the detector, all the vertical strip gains can be equalised. Moving the detector vertically will allow to do the same balancing for horizontal strips. This equalisation can be performed online from the energy histogram information for both the main calorimeter and the presampler.

Presampler and main calorimeter relative gains:
The coincidence with the Electron Tagger has to be used: a selection of the entrance position of the electrons in this detector fixes the energy of the incoming photons in the Photon Detector. An absolute calibration of the Electron Tagger is not necessary at this point. A minimisation of the resolution with respect to the relative weights of both components of the

Photon Detector enables to calculate the relative gains.

Absolute calibration:
The total energy spectrum from a low luminosity bunch crossing or from an electron pilot bunch is dominated by the single photon distribution. It drops very sharply at the nominal electron beam energy and the position of this drop provides the absolute energy scale.

Monitoring:
The optical calibration provides a powerful means of monitoring the light transmission in the fibres and the response of the photodetector and the complete electronics chain.

A laser or flash lamps (Xe or H) can be used as light sources for the main calorimeter and the presampler; the flash lamp is a cheap solution also providing higher pulse rates. The output of the light source is monitored by a PIN diode (or an Hybrid Photo-Diode (HPD) if a gain is needed), which is read out by the same electronics and also used as the optical calibration trigger.

Electronics calibration:
Such a calibration is necessary for the linearity measurement of the full electronic chain. A possible scheme, based on the electronics calibration developed for the ATLAS liquid argon calorimeter could be used; the voltage pulse, fed at the charge preamplifier input would be generated at the detector level, with a suitable shape in order to simulate the photo-detector current pulse.

The absolute calibration of the Electron Tagger is obtained from the fixed total energy sum in the Electron Tagger and the Photon Detector for incoming particles originating from the process (1).

7 Funding, responsibilities and time planning

7.1 Funding

A total funding of 400 kDM is foreseen by the institutes involved in the new luminosity system, covering the cost estimate of both detectors (PD and ET6) and electronics (see table 3). The cost estimate for the photon detector includes the photomultipliers. Cost estimates for the slow-control and the equipment correspond to improvements and adaptation of those of the present system.

ITEMS	Cost Estimate (kDM)
Photon Det.	170
Electron Det.	30
Electronics	150
Slow Control	20
Equipment	20

Table 3: Cost estimates of the 2000-Luminometer

7.2 Responsibilities and time planning

The responsibilities and the time-planning are summarised in the table 4. The end of the construction of both detectors is planned for mid-1999, in order to allow a beam test at CERN (SPS) during the summer 1999. The time-planning of the final electronics boards (shaper, ADC etc.) is the end of 1999. The new DAQ and its associated on-line software are foreseen also for this date. As a training bench, it is planned to replace, during the year 1998, the present 29K of the L0 system (ref. [21]) by the proposed Power PC boards and the L3 bus by the MFCC bus.

ITEMS	Responsibilities	Time Planning
Detectors PD ET6	 Ecole/LPI LPI/Ecole	 1998-99: Design, construction 1999: Beam test summer 99
Electronics DAQ	Ecole/LAL/P6	1998-99: Design, proto. ... 1999(End): Fully tested electronics
On-line Soft.	LPI/Ecole	End 1999
Slow Control	LPI	End 1999
Simulation	LPI/Ecole	Detectors: sept 1998 H1SIM: June 1999
North Hall: Installation Commissioning Maintenance	 All Institutes	 Start: January 2000 End: June 2000 End: 2006...
Running:	LPI/Ecole	Start: July 2000 End: 2006...

Table 4: Responsibilities and time planning

References

[1] H1 Collaboration, I. Abt *et al.*, "*The H1 detector at HERA.*," Nucl. Instrum. Meth. **A386** (1997) 310.

[2] H1 Collaboration, I. Abt *et al.*, "*Experimental Study of Hard Photon Radiation Processes at HERA*," Z. Phys. **C66** (1995) 529.

[3] L. Favart and R. Maracek, "*H1 1994 Integrated Luminosity Measurement Using Bremsstrahlung Overlapping Events and Quasi-Real QED Compton Events.*" H1-11/96-503.

[4] M. W. Krasny *et al.*, "*Determination of the longitudinal structure function at HERA from radiative events*," in *Proceedings of the Workshop on the Physics at HERA* (W. Buchmüller and G. Ingelmann, eds.), vol. 1, p. 171, DESY, Hamburg, 1991.

[5] W. Bartel *et al.*, "*HERA Luminosity Upgrade*," in *Proceedings of the Workshop 1995/96, DESY*, vol. 2, p. 1095, 1996.

[6] HERA Polarisation Group, "*Polarisation 2000.*" PRC proposal.

[7] H. A. Bethe and J. Ashkin, *Experimental Nuclear Physics*, vol. 1. John Wiley and Sons, Inc., 1953.

[8] C. Bini *et al.*, "*Fast measurements of luminosity at LEP by detecting the single bremsstrahlung photons*," Nucl. Instrum. Meth. **A306** (1991) 468.

[9] L. Landau and I. Pomeranchuk, "*Limits of applicability of the theory of bremsstrahlung electrons and pair production at high energies*," Dokl. Akad. Nauk Ser. Fiz. **92** (1953) 535–536.

[10] M. L. Perl, "*Notes on the Landau, Pomeranchuk, Migdal effect: Experiment and theory*,". SLAC-PUB 6514 (1994).

[11] L. Suszicki, "*Luminosity Monitoring, Photon Tagging and QED tests*," in *Proceedings of the HERA Workshop*, vol. 2, (Hamburg), p. 503, 1987.

[12] G. L. Kotkin *et al.*, "*Influence of the transverse beam sizes on the e p $\rightarrow$ e p gamma cross-section at the HERA and a future CERN electron - proton collider*," Z. Phys. **C39** (1988) 61.

[13] K. Piotrzkowski, "*Observation of the beam size effect at HERA*," Z. Phys. **C67** (1995) 577–584, `hep-ex/9504003`.

[14] S. Levonian and A. Panitch, "*Treatment of the Proton Satellite Bunches in 1994 Data.*" H1-09/95-454, 1995.

[15] A. Meseck. private communication.

[16] J. H. Hubbell, "*Photon Mass Attenuation and Energy-Absorption Coefficients from 1 keV to 20 MeV*," Int. J. Appl. Radiat. Isot. **33** (1982) 1269–1290.

[17] P. Gorodetzky *et al.*, "*Quartz fiber calorimetry*," Nucl. Instrum. Meth. **A361** (1995) 161–179.

[18] M. Lundin *et al.*, "*On the electromagnetic energy resolution of Čerenkov fiber calorimeters*," Nucl. Instrum. Meth. **A372** (1996) 359–367.

[19] S. Levonian, "*H1LUMI - A Fast Simulation Package for the H1 Luminosity system.*" H1-04/93-287.

[20] V. Andreev, "*Acceptance Determination of Electron Tagger (ET44) in 1995.*" H1-10/96-493.

[21] E. Barrelet, "*The L0 system.*" H1 note to be published.